





# Meshless Super-Resolution of Scattered Data via constrained RBFs and KNN-Driven Densification

Iacopo Tirelli<sup>1\*</sup>, Miguel Alfonso Mendez<sup>2,1</sup>, Andrea Ianiro<sup>1</sup>,  
Stefano Discetti<sup>1</sup>

<sup>1\*</sup>Department of Aerospace Engineering, Universidad Carlos III de Madrid, Avda. Universidad 30, Leganés, 28911, Madrid, Spain.

<sup>2</sup>Environmental and Applied Fluid Dynamics, von Karman Institute for Fluid Dynamics, Waterlooesteeweg 72, Sint-Genesius-Rode, 1640, Bruxelles, Belgium.

\*Corresponding author(s). E-mail(s): [iacopo.tirelli@uc3m.es](mailto:iacopo.tirelli@uc3m.es) ;  
Contributing authors: [mendez@vki.ac.be](mailto:mendez@vki.ac.be) ; [aianiro@ing.uc3m.es](mailto:aianiro@ing.uc3m.es) ;  
[sdiscett@ing.uc3m.es](mailto:sdiscett@ing.uc3m.es) 

## Abstract

We propose a novel meshless method to achieve super-resolution from scattered data obtained from sparse, randomly-positioned sensors such as the particle tracers of particle tracking velocimetry. The method combines K-Nearest Neighbor Particle Tracking Velocimetry (KNN-PTV, [Tirelli et al., 2023](#)) with meshless Proper Orthogonal Decomposition (meshless POD, [Tirelli et al., 2025](#)) and constrained Radial Basis Function regression (c-RBFs, [Sperotto et al., 2022](#)). The main idea is to use KNN-PTV to enhance the spatial resolution of flow fields by blending data from *locally similar* flow regions available in the time series. This *similarity* is assessed in terms of statistical coherency with leading features, identified by meshless POD directly on the scattered data without the need to first interpolate onto a grid, but instead relying on RBFs to compute all the relevant inner products. Lastly, the proposed approach uses the c-RBF on the denser scattered distributions to derive an analytical representation of the flow fields that incorporates physical constraints. This combination is *meshless* because it does not require the definition of a grid at any step of the calculation, thus providing flexibility in handling complex geometries. The algorithm is validated on **3D** measurements of a jet flow in air. The assessment covers three key aspects: statistics, spectra, and modal analysis. The proposed method is evaluated against standard Particle Image Velocimetry, KNN-PTV, and c-RBFs. The results demonstrate improved accuracy, with an average error on the order of **11%**, compared to

**13 – 14%** for the other methods. Additionally, the proposed method achieves an increase in the cutoff frequency of approximately  $\mathbf{3} - \mathbf{4}/\mathbf{D}$ , compared to the values observed in the competing approaches. Furthermore, it shows nearly half the errors in low-order reconstructions.

**Keywords:** KNN, c-RBFs, meshless algorithm, PTV, PIV

## 1 Introduction

The measurement of detailed quantitative field data of turbulent flows poses significant challenges due to the vast range of spatial and temporal scales involved, which widens with increasing Reynolds numbers. While Particle Image Velocimetry (PIV, Raffel et al., 2018) has become a robust tool for this purpose (Westerweel et al., 2013), its ability to resolve turbulent scales is constrained by both the sensor size and the inter-particle spacing in the images.

Although spatial resolution can potentially be improved by exploiting temporal consistency in short sequences (Sciacchitano et al., 2012, Schneiders et al., 2014), it seems that two-frame PIV has reached its physical limits in terms of dynamic spatial range. Kähler et al. (2012) demonstrated that, for average flow fields, the particle diameter imposes a key limitation on cross-correlation-based methods, confirming particle tracking as the most suitable approach to enhance spatial resolution. On instantaneous measurements, dense vector fields can be obtained with super-resolution Particle Tracking Velocimetry (super-resolution PTV, Keane et al., 1995), although its reliability is more dependent on image quality than standard cross-correlation. In this context, the term super-resolution refers to the integration of PTV within PIV interrogation windows, enabling velocity measurements that exceed the spatial resolution limits of traditional cross-correlation methods.

In super-resolution PTV, the spatial resolution is determined by the smaller mean spacing between particles and their displacement between light pulses. In 3D velocimetry, the superiority of particle tracking over cross-correlation is even more established than that of the planar counterpart. The lower computational cost of evaluation, the lower risk of ambiguity in particle pairing, and the use of multiple cameras that allow disambiguating particles overlapping in an image using other views are factors that play in favour of particle tracking.

It is nevertheless common practice to interpolate the data on a Eulerian grid for postprocessing and visualization. This process inevitably introduces unnecessary filtering effects and artifacts due to interpolation (Scarano, 2003), affecting the final accuracy of the measured flow fields.

In this work, we adopt and extend the meshless super-resolution framework introduced by Sperotto et al. (2022), Ratz and Mendez (2024), which seek to eliminate interpolation and grids from all post-processing steps in tracking velocimetry. In this framework, the notion of super-resolution refers to the derivation of a mesh-independent analytical representation of the velocity field, allowing predictions at any point while simultaneously enforcing physical constraints (e.g., no-slip condition, mass

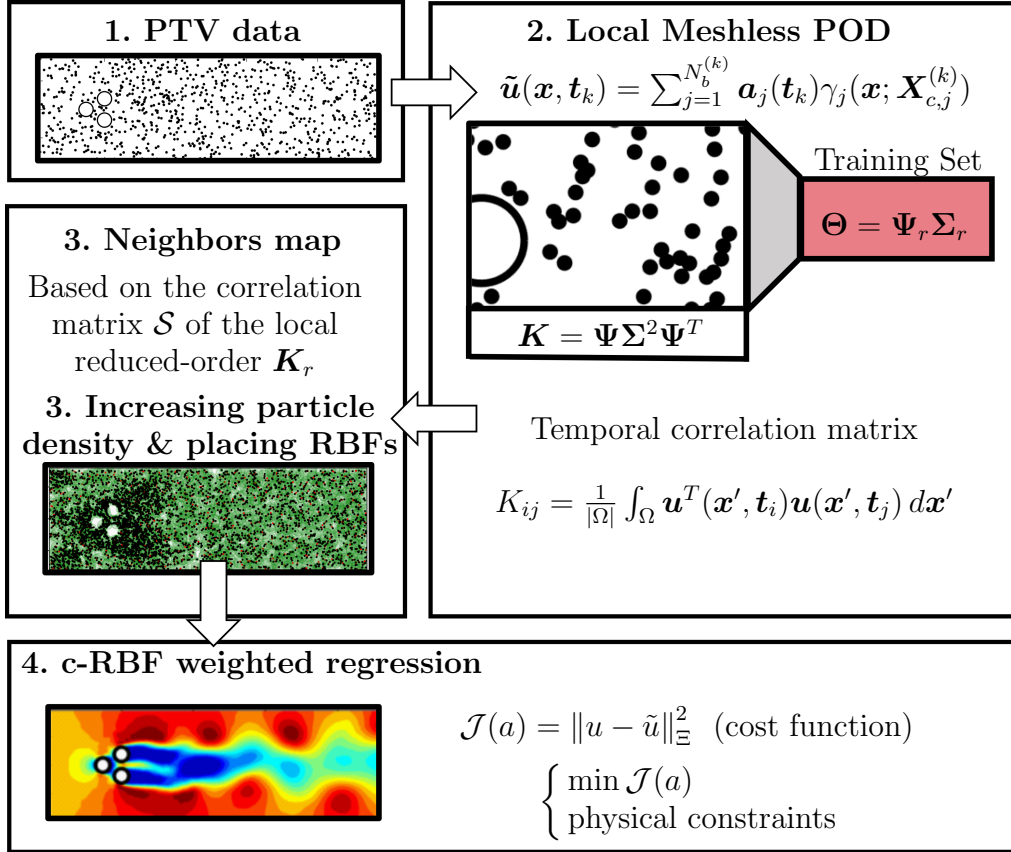


**Fig. 1** Flowchart of the proposed algorithm. Step 1: extraction of information from particles (PTV or LPT); step 2: local meshless POD directly on the particles within the subdomains into which the domain is partitioned; step 3: computing optimal number of neighbours and then increasing particle density; step 4: weighted regression through c-RBFs to achieve analytical high-resolution approximation of the velocity field.

conservation, etc.). This formalism is based on constrained Radial Basis Functions (c-RBFs) regression (Mendez et al., 2025), placed in the measurement domain and shaped in ways that account for seeding density inhomogeneities. Nevertheless, when processing instantaneous fields, the accuracy and feasibility of the method are constrained by particle availability. Regions with sparse sampling require larger RBFs, which can ultimately lead to significant low-pass filtering of the velocity field. The method proposed in this work offers a fully meshless approach to increase seeding density prior to a c-RBF regression.

A large class of methods leverages statistical evidence of correlation to increase the particle density in instantaneous realizations by “borrowing” information from other snapshots of the dataset. The underpinning of these methods stands upon recognizing that each velocity vector realization represents a sample from an underlying statistical

distribution. This principle gave rise to established techniques for resolution enhancement of turbulence statistics, see e.g. single-pixel correlation (Meinhart et al., 2000, Westerweel et al., 2004, Scharnowski et al., 2012) and ensemble PTV (Kähler et al., 2012, Cowen et al., 1997, Agüera et al., 2016). Recent advances in data-driven and machine-learning algorithms have led to push this concept to individual samples (Disceetti and Liu, 2022). A first effort in this direction was followed by Cortina-Fernández et al. (2021), who proposed a Data-Enhanced PTV (DEPTV). The main idea was that high-resolution Proper Orthogonal Decomposition (POD) modes can be obtained by progressively filling linear-stochastic estimates based on projection on a temporal basis obtained by standard PIV data analysis. The DEPTV assumes a linear mapping between low- and high-resolution basis. This hypothesis was progressively weakened by switching to locally-linear methods and fully nonlinear methods. In the first category, K-Nearest Neighbor Particle Tracking Velocimetry (KNN-PTV, Tirelli et al., 2023) stands out for its simplicity of implementation. KNN-PTV is based on the idea of blending particles from different snapshots when local regions are sufficiently similar. The similarity was assessed based on POD of the flow fields obtained by standard PIV analysis. Thus, intrinsically, the method relies on an Eulerian grid for its implementation. Nonlinear methods can provide better performances but have similar requirements, especially when using deep learning techniques such as Generative Adversarial Networks (Deng et al., 2019, Güemes et al., 2022) or estimators based on optical flow (Cai et al., 2019, Lagemann et al., 2021, Yu et al., 2021).

The existing methods suffer one or more of the issues in the following list: (1) difficulty in including physical constraints in the formulation; (2) restriction in the mapping capability when imposing linearity; (3) limited generalizability in conditions other than the training ones; and (4) rigidity on the choice of the grid, which cannot adapt to the scattering of the data.

In this work, we propose combining KNN-PTV with constrained regression using Radial Basis Function (RBF). On one hand, c-RBFs eliminate the need for a predefined grid in KNN-PTV. On the other hand, KNN-PTV artificially increases particle density in individual snapshots, generating denser scattered distributions that enable c-RBFs to produce physically constrained and highly accurate superresolution fields. The key novelty to achieve a fully meshless algorithm is the use of the recently proposed meshless POD (Tirelli et al., 2025) to evaluate the similarity between snapshots in the KNN-PTV. The features extracted from the meshless POD are less affected by spatial modulation errors and thus offer a more accurate definition of similarity.

The methodology is detailed in § 2. The experimental assessment on three-dimensional PTV measurements of a jet flow in air (described in § 3) is discussed in § 4 in terms of statistics (§ 4.1), spectra (§ 4.2) and modal analysis (§ 4.3).

## 2 Methodology

The workflow of the meshless KNN-PTV with c-RBFs is summarised in Fig. 1. As in the KNN-PTV proposed by Tirelli et al. (2023), the cornerstone of the super-resolution is the merging of particles belonging to different snapshots to artificially increase the particle density. Particles from different snapshots are merged only when

---

**Algorithm 1** Meshless KNN-PTV

---

**Require:** Data:  $\{\mathbf{u}(\mathbf{X}^{(i)}, \mathbf{t}_i)\}$  for  $i = 1, 2, \dots, N_t$  (scattered in space and time).

**Ensure:** High-resolution analytical flow fields.

---

*Step 1: Particle detection*

**Require:** particle image pairs or sequences.

**Ensure:** Particle distribution.

- 1: **for** each time step  $\mathbf{t}_i$  **do**
  - 2:     Perform PTV (Keane et al., 1995) or LPT (Schröder and Schanz, 2023).
  - 3: **end for**
- 

*Step 2: Local Meshless POD (Tirelli et al., 2025)*

**Require:** Data:  $\{\mathbf{u}(\mathbf{X}^{(i)}, \mathbf{t}_i)\}$  for  $i = 1, 2, \dots, N_t$  (scattered in space and time).

**Ensure:** Training set  $\Theta = \Psi_r \Sigma_r$ .

- 4: **for** each subdomain **do**
  - 5:     **for** each time instant  $t_k$  **do**
  - 6:         Compute analytical approximation through RBF:  $\tilde{\mathbf{u}}(\mathbf{x}, t_k) = \sum_{j=1}^{N_b^{(k)}} \mathbf{a}_j(t_k) \gamma_j(\mathbf{x}; \mathbf{X}_{c,j}^{(k)})$ .
  - 7:     **end for**
  - 8:     Compute temporal correlation matrix:  $\mathbf{K} \in \mathbb{R}^{N_t \times N_t}$ .
  - 9:     Decompose  $\mathbf{K}$  through SVD:  $\mathbf{K} = \Psi \Sigma^2 \Psi^T$
  - 10:     Assemble training set  $\Theta = \Psi_r \Sigma_r$ , with  $r$  the number of modes that retain the 90% of the energy.
  - 11: **end for**
- 

*Step 3: Enriching snapshots and RBFs placing*

**Require:** Data:  $\{\mathbf{u}(\mathbf{X}^{(i)}, \mathbf{t}_i)\}$  for  $i = 1, 2, \dots, N_t$ ; local training set  $\Theta$ .

**Ensure:** Enriched snapshots.

- 12: **for** each high-resolution snapshot needed **do**
  - 13:     **for** each subdomain **do**
  - 14:         Compute correlation matrix  $\mathbf{S} = \mathbf{K}_r \oslash (\kappa \kappa^T)$
  - 15:         Compute the number of neighbours  $k$  as the number of element in  $\mathbf{S}$  higher than a given threshold
  - 16:         Increase local particle density according to  $k$  via KNN
  - 17:     **end for**
  - 18:     Iterative agglomerative clustering to place collocation points and corresponding RBFs (Sperotto et al., 2022)
  - 19: **end for**
- 

*Step 4: RBF constrained weighted regression*

**Require:** Enriched snapshots, collocation points, training set.

**Ensure:** High-resolution analytical flow fields

- 20: Compute weighting matrix  $\Xi$
  - 21: **for** each high-resolution snapshot needed **do**
  - 22:     Perform RBF weighted regression on the enriched particle distribution (solving the system in Eq. (10))
  - 23: **end for**
-

a local similarity is identified. For this purpose, the domain is divided into subdomains and, for each of them at each time instant, the algorithm searches for the most locally similar realizations within the data ensemble. If the flow fields in a subdomain at different time instants are deemed sufficiently similar, their particles are merged to create a denser snapshot. The similarity is assessed here by a local meshless POD (Tirelli et al., 2025). The data is then used to feed a constrained interpolator based on RBFs (Sperotto et al., 2022) to obtain an analytical description of the flow field. The algorithm consists of 4 main steps, outlined in the following and listed in Algorithm 1.

### Step 1: Particle detection

The first step involves extracting information from particles using conventional PTV methods (Keane et al., 1995) or more modern Lagrangian Particle Tracking (LPT) algorithms, such as Shake-The-Box (STB). In the implementation presented in this manuscript, particle identification and pairing are performed with a traditional PTV algorithm. However, employing a more accurate tracking algorithm, such as STB, is anticipated to enhance the performance. For example, tracks obtained from STB could be used to enforce temporal coherence in the regression process. However, minor improvements are expected for time-resolved sequences, in which well-assessed methods of pouring time resolution into space can be used instead (Sciacchitano et al., 2012, Schneiders et al., 2014, Schneiders and Scarano, 2016).

### Step 2: Local Meshless POD

Meshless POD is used in this step to assess the similarity locally. The meshless POD introduced by Tirelli et al. (2025) eliminates the dependence on an Eulerian grid to define this set of local feature dictionaries and mitigates the bias error introduced by the interpolation of scattered data. In the meshless POD, the scattered velocity fields are approximated and replaced by analytical functions computed at each time instant  $\mathbf{t}_k$ . This approximation, denoted as  $\tilde{\mathbf{u}}(\mathbf{x}, \mathbf{t}_k)$ , is defined as a linear combination of RBFs:

$$\tilde{\mathbf{u}}(\mathbf{x}, \mathbf{t}_k) = \sum_{j=1}^{N_b^{(k)}} \mathbf{a}_j(\mathbf{t}_k) \gamma_j(\mathbf{x}; \mathbf{X}_{c,j}^{(k)}), \quad (1)$$

where  $\mathbf{a} \in \mathbb{R}^{N_b^{(k)}}$  is the vector collecting the weight that identifies the best approximation, and  $\gamma_j(\mathbf{x}; \mathbf{X}_{c,j}^{(k)})$  is the basis function  $j$  of the location positioned at the collocation point  $\mathbf{X}_{c,j}^{(k)}$  available at the  $k^{\text{th}}$  time instant. For this step, we favour interpolative over regressive RBFs and thus collocate the bases at the particle locations. Therefore,  $N_b^{(k)}$  coincides with the number of particles in snapshot  $k$ . Moreover, following Tirelli et al. (2025), this step uses thin-plate spline (Buhmann, 2000) to reduce the number of tuning parameters. These bases have no shape factor and are defined as

$$\gamma_j(\mathbf{x}; \mathbf{X}_{c,j}^{(k)}) = \gamma_j(r(\mathbf{x}; \mathbf{X}_{c,j}^{(k)})) = r^2 \log(r), \quad (2)$$

with  $r = \|\mathbf{x} - \mathbf{X}_{c,j}^{(k)}\|$  the distance from the collocation point.

The POD is performed on the analytical approximation of the mean-shifted velocity fields of Eq. (1). The inner product over the spatial domain of all velocity field

approximations is used to compute the temporal correlation matrix  $\mathbf{K}$ , defined in terms of continuous inner product (Lumley, 1967) as:

$$K_{ij} = \frac{1}{|\Omega|} \int_{\Omega} \mathbf{u}^T(\mathbf{x}', t_i) \mathbf{u}(\mathbf{x}', t_j) d\mathbf{x}', \quad (3)$$

with  $|\Omega|$  the area (in 2D) or volume (in 3D) of the spatial domain considered. The decomposition of the matrix  $\mathbf{K}$  produces the temporal modes and their corresponding eigenvalues.

The analytic approximation provided by (1) allows for using quadrature methods to compute the integral in (3) with quadrature points, eliminating the need to interpolate data on a mesh. This reduces spatial modulation effects and enhances decomposition accuracy. The reader is referred to Tirelli et al. (2025) for more details on the meshless POD. The meshless POD is applied to all the subdomains to extract local sets of coordinates. These are then used to construct a local feature training set, denoted as  $\Theta = \Psi_r \Sigma_r \in \mathbb{R}^{N_t \times r}$ , consisting of the temporal modes and the eigenvalues of the subdomain truncated at rank  $r$ , which is the number of modes that retain the 90% of the energy.

### Step 3: Enriching snapshots and RBFs placing

The third step involves determining the optimal number of neighbours for each subdomain based on the number of sufficiently (locally) similar snapshots in the dataset. The correlation between different time instants of each subdomain is employed as a metric.

Using the continuous inner product, the correlation for the specific subdomain at two different time instants  $i$  and  $j$ , is given by:

$$\mathcal{S}_{ij} = \frac{\int_{\Omega} \mathbf{u}(\mathbf{x}, t_i) \mathbf{u}(\mathbf{x}, t_j) d\mathbf{x}}{\sqrt{\int_{\Omega} \mathbf{u}(\mathbf{x}, t_i)^2 d\mathbf{x}} \sqrt{\int_{\Omega} \mathbf{u}(\mathbf{x}, t_j)^2 d\mathbf{x}}}. \quad (4)$$

This matrix can be obtained from the diagonal normalization of the matrix  $\mathbf{K}$

$$\mathcal{S} = \mathbf{K} \oslash (\boldsymbol{\kappa} \boldsymbol{\kappa}^T), \quad (5)$$

where  $\boldsymbol{\kappa} \in \mathbb{R}^{N_t}$  collects the square root of the diagonal elements of  $\mathbf{K}$  and  $\oslash$  is the Hadamard division (entry by entry).

In this step, the similarity is assessed in the reduced-order version of  $\mathbf{K}$ , obtained retaining only the  $r$  modes accounting for the 90% of the energy. The number of local neighbours  $k$  is given by the number of elements in each row of  $\mathcal{S}$  that exhibits a similarity higher than a certain threshold.

This step replaces the need to create a reduced training set to search for the optimal number of neighbours  $k$ , which was the most computationally expensive part of the implementation in Tirelli et al. (2023). In addition to reducing computational costs, the proposed approach also allows for the adaptation of  $k$  for different time instants.

It is worth noting that this step only determines the number of neighbours, not their positions. The positions are subsequently found using the KNN algorithm, which

operates in the more refined feature space provided by the mesh-free modes. This process is repeated independently for each local subdomain, resulting in a comprehensive neighbour map in space and time.

The particle density is then artificially increased according to this map, borrowing particles from the  $k$  nearest neighbours. Subsequently, the collocation points needed for the regression are placed through iterative agglomerative clustering as in [Sperotto et al. \(2022\)](#).

#### Step 4: RBF constrained weighted regression

The analytical high-resolution flow fields are obtained using the c-RBFs framework, as introduced by [Sperotto et al. \(2022\)](#), with modifications to enhance compatibility with KNN-PTV. Unlike in Step 2, this approach employs regressive RBFs with isotropic Gaussian basis functions  $\varphi$ :

$$\varphi_j(\mathbf{x}; \mathbf{X}_{c,j}^{(k)}) = e^{-c^2 \|\mathbf{x} - \mathbf{X}_{c,j}^{(k)}\|_d^2}. \quad (6)$$

The term ‘‘isotropic’’ refers to the fact that  $c > 0$  is the only shape parameter governing the basis function.

In the framework of this work, the scattered data from PTV or LPT can be seen as samples of the analytical function of the 3D flow field  $\mathbf{u}(\mathbf{x}) = (u(\mathbf{x}), v(\mathbf{x}), w(\mathbf{x}))$ , which is to be approximated by the linear system:

$$\begin{aligned} \mathbf{u}(\mathbf{X}^{(k)}, t_k) &= \begin{pmatrix} u(\mathbf{X}^{(k)}, t_k) \\ v(\mathbf{X}^{(k)}, t_k) \\ w(\mathbf{X}^{(k)}, t_k) \end{pmatrix} \approx \begin{pmatrix} \Phi_b(\mathbf{X}^{(k)}) & 0 & 0 \\ 0 & \Phi_b(\mathbf{X}^{(k)}) & 0 \\ 0 & 0 & \Phi_b(\mathbf{X}^{(k)}) \end{pmatrix} \begin{pmatrix} \mathbf{a}_u(t_k) \\ \mathbf{a}_v(t_k) \\ \mathbf{a}_w(t_k) \end{pmatrix} \\ &= \Phi(\mathbf{X}^{(k)})\mathbf{A}(t_k). \end{aligned} \quad (7)$$

where  $\Phi_b(\mathbf{X}^{(k)}) \in \mathbb{R}^{N_p(k) \times N_b(k)}$  is the short-hand notation for  $\Phi_b(\mathbf{X}^{(k)} | \mathbf{X}_c^{(k)}, \mathbf{c})$ , obtained by evaluating the  $N_b$  basis functions on the set of coordinates  $\mathbf{X}^{(k)}$  with respect to the centers  $\mathbf{X}_c^{(k)} \in \mathbb{R}^{N_p(k) \times 3}$  and the vector of shape factors  $\mathbf{c} \in \mathbb{R}^{N_b}$ .

In the constrained formalism introduced by [Sperotto et al. \(2022\)](#), quadratic penalties and linear constraints can be incorporated. Penalties act as ‘‘soft constraints’’, promoting the minimization of quadratic terms, while constraints are enforced through Lagrange multipliers  $\lambda$ . The use of linear penalties and quadratic constraints ensures that the associated augmented cost function, built to satisfy the Karush-Kuhn-Tucker optimality condition, remains in a quadratic form. The main interest in using both penalties and constraints is to strike a balance between computational cost and accuracy. Penalties do not increase the size of the training problem but do not guarantee the fulfilment of the penalized conditions, while constraints ensure the fulfilment of the imposed conditions at the specified points but introduce an additional unknown for each constraint at each point.

The novelty compared to the original implementation by [Sperotto et al. \(2022\)](#) lies in the application of regression to an enriched particle distribution. This requires introducing a weighting metric in the regression process to account for the fact that



some particles do not originate from the current snapshot but are instead from their neighbours, which may have varying degrees of similarity to the current snapshot under consideration.

By slightly modifying the implementation in the open-source toolbox SPICY (Mendez et al., 2025, Sperotto et al., 2024), the final cost function to be minimized, incorporating constraints such as Dirichlet and Neumann boundary conditions, as well as the solenoidal condition implemented both as penalty and constraint reads:

$$\begin{aligned} \mathcal{J}(\mathbf{a}, \boldsymbol{\lambda}) = & \| \mathbf{U}(\mathbf{X}) - \boldsymbol{\Phi}(\mathbf{X})\mathbf{A} \|_{\Xi}^2 + \boldsymbol{\lambda}_D^T (\mathbf{D}(\mathbf{X}_D)\mathbf{A} - \mathbf{c}_D) + \boldsymbol{\lambda}_N^T (\mathbf{N}(\mathbf{X}_N)\mathbf{A} - \mathbf{c}_N) \\ & + \boldsymbol{\lambda}_{\nabla}^T (\mathbf{D}_{\nabla}(\mathbf{X}_{\nabla})\mathbf{A}) + \alpha_{\nabla} \| \mathbf{D}_{\nabla}(\mathbf{X}_g)\mathbf{A} \|_2^2. \end{aligned} \quad (8)$$

The first term  $\| \mathbf{U}(\mathbf{X}) - \boldsymbol{\Phi}(\mathbf{X})\mathbf{A} \|_{\Xi}^2$  is the weighted norm with respect to  $\Xi$ . The diagonal weighting matrix  $\Xi$  is used here to penalise the information provided by other snapshots. The penalisation term is based on the distance in the local feature space  $\Theta$ . The matrix  $\Xi_{ij}$  is computed as:

$$\Xi = e^{-(\alpha \frac{\mathbf{D}}{\|\Theta\|})^2} \in \mathbb{R}^{N_t \times N_t}. \quad (9)$$

Similar to what is described in Tirelli et al. (2023), this weighting coefficient accounts for the distances  $\mathbf{D}$  in the feature space, normalized by the norm of the feature set and penalized by a factor  $\alpha$ .

In this step, physical constraints are also enforced to better suit the specific case study, as shown in Eq. (8). The second, third and fourth terms on the right-hand side are the linear operators associated with the imposition of Dirichlet, Neumann and divergence-free conditions, applied to  $\mathbf{X}_D \in \mathbb{R}^{N_D}$ ,  $\mathbf{X}_N \in \mathbb{R}^{N_N}$  and  $\mathbf{X}_{\nabla} \in \mathbb{R}^{N_{\nabla}}$  respectively, modelled as in Sperotto et al. (2022). The last term is a soft constraint used to penalize the violation of the divergence-free condition, acting on  $\mathbf{X}_g \in \mathbb{R}^{N_g}$  and weighted by the parameter  $\alpha_{\nabla} \in \mathbb{R}^+$ .

Another difference with the original framework, is that here only Gaussian basis functions have been employed. More complex RBFs can be easily integrated into the proposed framework. It is important to emphasize that the selection of basis functions does not affect the generality of the formulation. Despite the well-known significant role that polynomial basis could play in terms of regularization of the regression and approximation of global behaviour, as shown in Sperotto et al. (2022), it is also acknowledged that its effectiveness heavily relies on the expertise of the user. This is crucial as the correct scaling of the domain is required to position them optimally. Inspired by the concept of the first KNN-PTV, aiming for an end-to-end tool that starts from raw images and yields output with minimal user intervention, the polynomial function has been excluded. This decision, while sacrificing a degree of accuracy, reduces the number of parameters to be selected. Future investigations will focus on identifying a set of bases that strikes the best compromise between accuracy and simplicity.

The minimization of Eq. (8) with respect to the RBFs weights and the Lagrange multipliers associated with the constraints leads to the following system of equations:

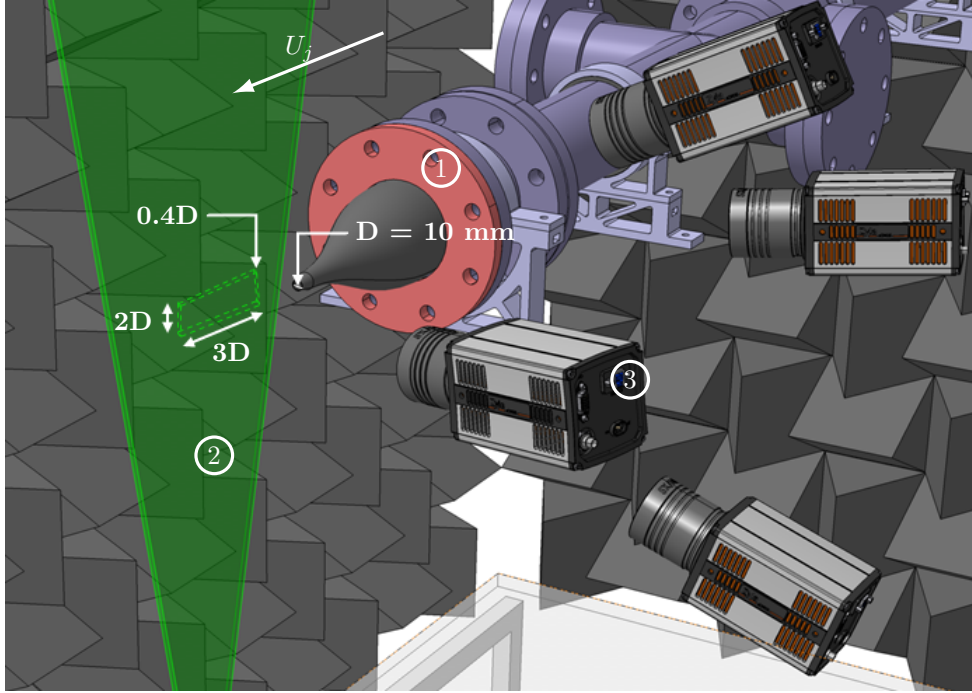


**Fig. 2** Sketch of the experimental setup. (1) jet nozzle; (2) Ng:Yag Quantel Evergreen laser; (3) ANDOR Zyla sCMOS 5.5 MP camera.

$$\begin{pmatrix} \mathbf{\Gamma} & \mathbf{\Delta} \\ \mathbf{\Delta}^T & \mathbf{0} \end{pmatrix} \begin{pmatrix} \mathbf{A} \\ \boldsymbol{\lambda} \end{pmatrix} = \begin{pmatrix} \mathbf{b}_1 \\ \mathbf{b}_2 \end{pmatrix}, \quad (10)$$

where  $\boldsymbol{\lambda} = (\boldsymbol{\lambda}_D, \boldsymbol{\lambda}_N, \boldsymbol{\lambda}_\nabla) \in \mathbb{R}^{n_\lambda}$ , with  $n_\lambda = 3n_D + 3n_N + n_\nabla$  the total number of constraints. The matrices  $\mathbf{\Gamma}$  and  $\mathbf{\Delta}$ , along with the vectors  $\mathbf{b}_1$  and  $\mathbf{b}_2$ , are defined as follows:

$$\mathbf{\Gamma} = 2\boldsymbol{\Phi}^T(\mathbf{X})\boldsymbol{\Xi}^T\boldsymbol{\Xi}\boldsymbol{\Phi}(\mathbf{X}) + 2\alpha_\nabla\mathbf{D}_\nabla^T(\mathbf{X})\mathbf{D}_\nabla(\mathbf{X}) \in \mathbb{R}^{3N_b \times 3N_b} \quad (11a)$$

$$\mathbf{\Delta} = (\boldsymbol{\Phi}_b^T(\mathbf{X}_D); \mathbf{N}_n^T(\mathbf{X}_N); \mathbf{D}_\nabla^T(\mathbf{X}_\nabla)) \in \mathbb{R}^{3N_b \times N_\lambda} \quad (11b)$$

$$\mathbf{b}_1 = 2\boldsymbol{\Phi}^T(\mathbf{X})\boldsymbol{\Xi}^T\boldsymbol{\Xi}\mathbf{U}(\mathbf{X}) \in \mathbb{R}^{3N_b} \quad (11c)$$

$$\mathbf{b}_2 = (c_D; c_N; \mathbf{0}) \quad (11d)$$

The final output of this step is a set of weights that enables the visualization of the analytical field on any grid while preserving the super-resolution achieved regardless of the underlying discretization.

### 3 Experimental dataset: 3D jet flow

The experimental validation aims to complete the process initiated with the first version of KNN-PTV. The assessment results reported in [Tirelli et al. \(2023\)](#) indicate that, although this algorithm produced encouraging outcomes, it struggled with larger

PIV IW 128	KNN-PTV	c-RBF	meshless KNN
0.1395	0.1332	0.1215	0.1133

**Table 1** Spatial average of the root mean square error  $\langle \delta_{RMS} \rangle$  evaluated for: PIV with interrogation window of 128 pixels, KNN-PTV. c-RBF and meshless KNN-PTV.

interparticle spacing and increasing computational costs. This motivated the incorporation of RBFs, enabling the algorithm to adapt to 3D scenarios while maintaining reasonable computational expenses. For this reason, the experimental validation proposed in this work is carried out on the same 3D jet flow of the above-mentioned paper.

The experiments are conducted in the jet flow facility located in the anechoic chamber of UC3M, as sketched in Fig 2. The jet has a nozzle diameter of 10 mm and is issued at a bulk velocity of 11.2 m/s, resulting in a Reynolds number  $Re = 7,500$ . DEHS particles, approximately  $1 \mu\text{m}$  in diameter, are used to seed the jet. A Nd:Yag pulsed laser, with a maximum pulse power of 200 mJ and a repetition rate of 15 Hz, illuminates the particles. A domain of  $50 \times 45 \times 6.5 \text{ mm}^3$  (with the second dimension aligned along the axis of the jet) is imaged by four Andor Zyla sCMOS cameras (5.5 Mpx sensor,  $6.5 \mu\text{m}$  pixel pitch). These cameras are equipped with objectives that have a focal length of 100 mm and are set at  $f_{\#} = 11$ . The four cameras are arranged in a cross-like configuration within the same plane, with an opening angle of  $30^\circ$  in both directions.

The images undergo preprocessing using eigenbackground removal (Mendez et al., 2017) and a sliding minimum subtraction technique to set the background to zero. The self-calibration procedure introduced by Wieneke (2008) reduces the residual calibration error to below 0.1 pixels. A tomographic reconstruction process (Elsinga et al., 2006) is performed using a multi-resolution method (Discetti and Astarita, 2012) on a volume discretized with 28 voxels/mm. The process involves three camera-simultaneous multiplicative algebraic reconstruction technique (cSMART) iterations on a  $2 \times$  binned configuration, followed by three additional cSMART iterations and three SMART iterations at the final resolution of 11 voxels/mm. The cSMART is a modified version of the SMART procedure proposed by Atkinson and Soria (2009) which uses the cameras sequentially.

Individual particles are identified in the reconstructed volume and paired, in accordance with the Tomo-PTV principle established by Novara and Scarano (2013). A fast predictor is constructed using the sparse cross-correlation algorithm implemented by Discetti and Astarita (2012). A total of 1,000 snapshots have been processed.

Approximately 10,000 particles are accurately paired for each snapshot. This relatively low concentration is set to ensure a highly accurate reconstruction and a minimal occurrence of outliers, resulting in roughly 8 vectors in a  $64^3$  voxel volume. The complete distribution of vectors is used to create a reference "ground truth" field by weighting the moving average of the vector distribution with a Gaussian window, where the standard deviation is equal to  $64/1.5$  voxels. The approaches evaluated here are tested on an artificially downsampled vector distribution, containing only 1,000 particles distributed within the volume. Low-resolution fields are constructed using a

moving average over windows of  $128^3$  voxels, which contain, on average, 6.5 particles in the sparse particle distributions.

The mesh-free flow fields are generated by distributing the RBF basis across eight levels of clustering, ensuring a minimum number of particles per Gaussian of 2,3,4,5,6,10,30 and 50 respectively, leading to an average value of 4,000 basis for the enriched fields and almost the half for the traditional c-RBFs. Additionally, 1/10 of the original particles are constrained to satisfy the divergence-free condition, which is further enforced as a penalty in the regression process.

The validation process is conducted within a reduced domain of interest, defined by the ranges  $0.3D < x/D < 3.3D$ ,  $-1D < y/D < 1D$  and  $-0.2D < z/D < 0.2D$ . This selection ensures consistent particle coverage and well-converged results throughout the analyses.

## 4 Results

This section presents the validation of the algorithm on the experimental 3D jet flow. The results are compared with the following.

- **PIV IW = 128**: represents the standard approach in the field, obtained via a moving average with an interrogation window (IW) size of 128 voxels;
- **KNN-PTV**: the first version of the algorithm as proposed by [Tirelli et al. \(2023\)](#), included to highlight the improvements introduced by the meshless paradigm;
- **c-RBF**: meshless interpolation as in [Sperotto et al. \(2022\)](#); it isolates the benefits of introducing particles from other snapshots.

The comparison of the meshless KNN-PTV against these approaches aims to demonstrate the advantages of the proposed combination. On one hand, the ensemble approach introduced by KNN-PTV enables higher spatial resolution, which is further enhanced and preserved through the analytical approximation of RBFs. On the other hand, the fully meshless nature of the method relies solely on particle positions, effectively avoiding modulation effects introduced by discretization on Eulerian grids at any step.

The assessment is carried out across three key aspects: statistical, spectral, and modal analyses.

The statistical analysis in §4.1 includes ensemble and instantaneous statistics. For ensemble statistics, an additional reference is introduced: the EPTV approach developed by [Agüera et al. \(2016\)](#), using a bin size of 48 voxels. This method represents the state-of-the-art algorithm for ensemble statistics in PIV and serves as a further benchmark for comparison. For the spectral analysis, presented in §4.2, the goal is to evaluate and compare the frequency modulation introduced by all methods.

Finally, in terms of modal analysis, presented in §4.3, the goal was to evaluate the consistency of spatial modes as well as the convergence performances at varying ranks.

In the analysis that follows, the velocity fields of the PIVs and KNN-PTV are filtered using the criterion proposed by [Raiola et al. \(2015\)](#). In contrast, the RBF-based approaches did not benefit significantly from this filtering, likely because the

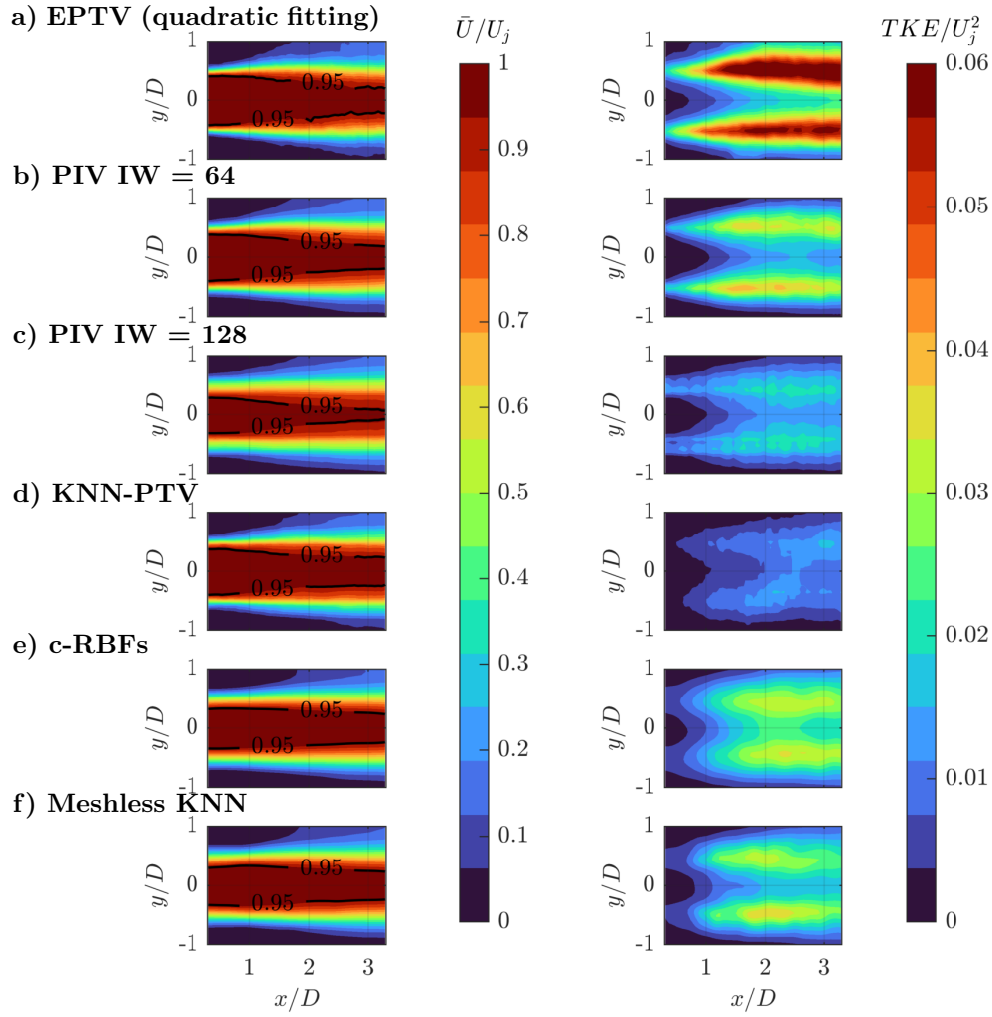


**Fig. 3** Mean velocity field (left column) and resultant standard deviation  $\sigma$  squared (right column): a) Ensemble averaging (Agüera et al., 2016) with bin size  $48 \times 48 \times 48$  pixels, b) PIV with interrogation window of  $64 \times 64 \times 64$  pixels, c) PIV with interrogation window of  $128 \times 128 \times 128$  pixels, d) KNN-PTV, e) c-RBFs and f) meshless KNN-PTV. Reference plane:  $z/D = 0$ . In black isolines for  $\bar{U}/U_j = [0.9, 0.5]$ .

constrained regression already regularizes the fields. Therefore, in these cases, the filter has not been applied.

#### 4.1 Statistical analysis

First- and second-order statistics are reported in Figure 3. The comparison panel depicts the mean flow along the streamwise direction on the left and the turbulent

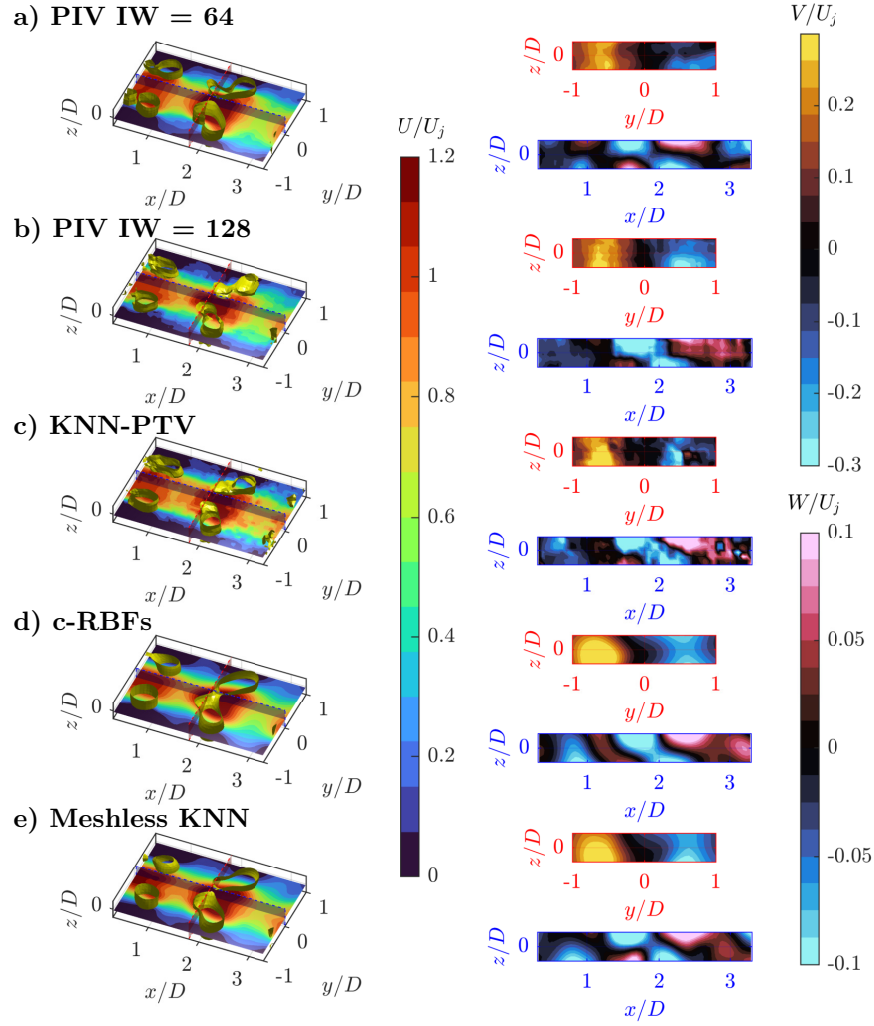


**Fig. 4** Instantaneous streamwise (first column), spanwise (second column, top) and crosswise (third column, bottom) velocity field contours for the middle planes: a) reference PIV with interrogation window of  $64 \times 64 \times 64$  pixels, b) PIV with interrogation window of  $128 \times 128 \times 128$  pixels, c) KNN-PTV, d) c-RBFs and d) meshless KNN-PTV. In yellow, the Q-criterion visualization for positive values of  $Q$ , smoothed using the Savitzky-Golay filter.

kinetic energy (TKE) on the right, both in the plane  $z/D = 0$  and normalized with the bulk velocity  $U_j$ .

In addition to the reference PIV with  $IW = 64$  voxels, only for the comparison of ensemble statistics, the EPTV approach developed by [Agüera et al. \(2016\)](#), with a bin size of 48 voxels (Fig. 3.a-left) is here used as further reference. The main differences in the mean flow arise from the analysis of the core region, highlighted by the black isolines at  $\bar{U}/U_j = 0.95$ : the PIV with  $IW = 128$  voxels (Fig. 3.b-left) is the only one whose core extension is shorter. This is probably due to the low availability of particles

combined with the large moving average window that is over-filtering the field. The RBF-based approaches (Fig. 3.e, f-left) exhibit a contraction of the region slightly less pronounced than the references (Fig. 3.a,b-left) and KNN-PTV (Fig. 3.d-left).

The main discrepancies emerge from the comparison of the TKE plots. The EPTV exhibits the highest peaks in the shear layer (Fig. 3.a-right). However, in the PIV with  $IW = 64$  voxels (Fig. 3.b-right), despite being computed with the same number of particles (10,000), these peaks are smoothed out due to the larger window used for the moving average. Similarly, the PIV with  $IW = 128$  voxels (Fig. 3.c-right) shows a comparable pattern but with even more filtering, resulting from the combination of lower particle availability and a larger interrogation window. The KNN-PTV (Fig. 3.d-right), while producing an accurate mean field, has the poorest performance in terms of TKE. This is attributed to the inability of the algorithm to capture the smallest fluctuations. Three primary factors contribute to this: low particle availability in each snapshot, limited number of samples, and large interparticle spacing. Together, these factors limit the ability of KNN-PTV to find close neighbours for merging, thereby failing to resolve the smallest scales. On the other hand, the mean flow remains unaffected because the largest scales, which dominate the mean flow, are successfully captured. Lastly, the RBF-based methods (Fig. 3.e, f-right) recover the majority of the energy. Notably, the addition of particles provided by the KNN offers a slight boost to the already well-converged results of the c-RBFs. This enhancement enables the placement of smaller but well-supported Gaussian bases, thereby facilitating the accurate modelling of the smallest scales.

A qualitative comparison of the instantaneous field is shown in Fig. 4. In all test cases, contours of the instantaneous streamwise (left column), spanwise (right column - top) and crosswise (right column - bottom) velocity field for the corresponding middle planes ( $z/D = 0$ ,  $y/D = 0$  in blue and  $x/D = 1.7D$  in red) are displayed. In yellow, positive values of  $Q$ -criterion visualization (Hunt et al., 1988) are reported, slightly smoothed using the Savitzky-Golay filter for visualization purposes (Savitzky and Golay, 1964).

Comparing the PIV results with an interrogation window of 128 voxels (Fig. 4.b) to the reference (Fig. 4.a), the former appears as a lower resolution version due to the lack of particles and larger moving averaging windows, that implies high smoothing effects on the field. The KNN-PTV implementation (Fig. 4.c) seems to recover smaller scales more effectively at first glance but suffers more noise contamination. The introduction of RBF seems to help regularize the flow field, making it appear smoother, as evident in Fig. 4.d. The level of detail is increased thanks to the availability of particles borrowed from other snapshots, as shown in Fig. 4.e.

These qualitative findings are confirmed by the error maps shown in Fig. 5. Here the root mean square error  $\delta_{RMS}$  has been employed as a metric, normalized with  $U_j$  and computed as:

$$\delta_{RMS} = \frac{\|\mathbf{u} - \mathbf{u}_{ref}\|}{\sqrt{N_t} U_j}, \quad (12)$$

where the reference is always the PIV with  $IW = 64$  voxels.

These maps, evaluated at  $z/D = 0$ , reveal that the highest errors occur near the shear layer region, reflecting the patterns observed in the TKE plots of Fig. 3-right. In

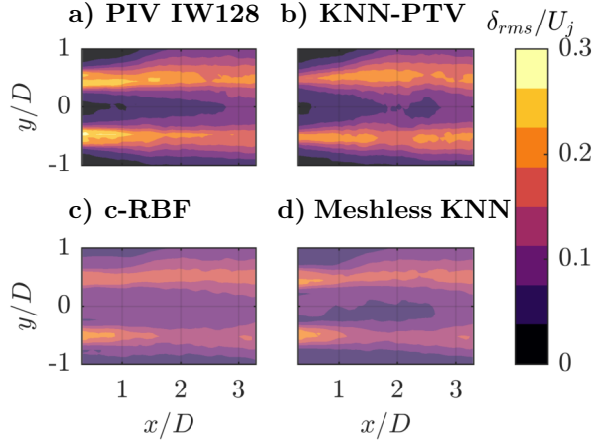


**Fig. 5** Spatial distribution of  $\delta_{RMS}$  normalized with  $U_\infty = 12$  m/s for the plane at  $z/D = 0$ : a) PIV with interrogation window of  $128 \times 128 \times 128$  pixels, b) KNN-PTV, c) c-RBFs and d) meshless KNN.

Fig. 5.a, the error peaks are concentrated in the shear layer closer to the exit, between  $x/D = 0.3D$  and  $1D$ , while the core region remains less affected, likely due to the lower variability in velocity fluctuations. These peaks are smoothed in the KNN-PTV results (Fig. 5.b), thanks to the artificial increase of particle density, which aids in capturing smaller fluctuations. The introduction of RBFs further decreases the peaks and reduces the average error, although this comes with slightly elevated errors in the core region (Fig. 5.c). The combination of these two methodologies achieves the best balance and overall performance, as confirmed by the spatial average of these maps in Tab. 1.

## 4.2 Spectral analysis

The streamwise velocity spectra are presented in Fig. 6 in terms of Power Spectral Density (PSD). The PSD is computed for a velocity profile at  $y/D = 0.5$  within the shear layer, evaluated at 11 equispaced stations along the  $z$ -direction and then averaged. This analysis is performed independently for all three velocity components.

The energy spectra of the reconstructed fields are compared with the reference PIV (in black). In general, the meshless KNN-PTV (light blue line) provides results closest to the reference. The c-RBFs (yellow line) exhibit a similar pattern, although performing slightly worse than the meshless KNN-PTV in the range  $1/D < f < 3/D$ , particularly evident in the streamwise component analysis. This is due to the filtering effect of using a larger kernel for the RBFs, while the meshless KNN-PTV can use smaller kernels due to the artificially-increased particle image density. The KNN-PTV as in the implementation by Tirelli et al. (2023), depicted with a light green line, follows the reference reasonably well up to a certain frequency ( $\approx 3/D$ ), displaying more stable behaviour compared to the PIV with an interrogation window of 128 pixels (red line), that tends to an oscillatory behaviour. However, the spectra deviate at high frequencies due to increased noise.



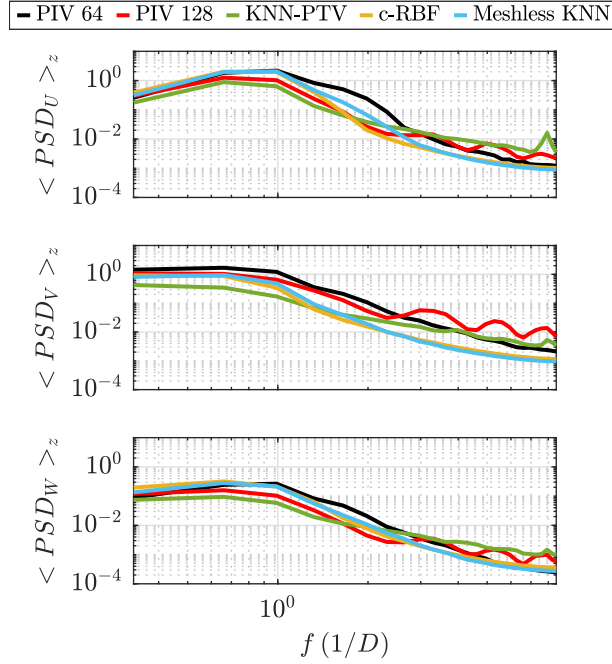


**Fig. 6** Power spectral density comparison at  $y/D = 0.5$ , averaged at different  $z/D$ : streamwise component  $U$  (first row), spanwise component  $V$  (second row), and crosswise component  $W$  (third row). The methodologies compared include: PIV IW = 64 (reference, black); PIV IW = 128 (red); KNN-PTV (light green); c-RBF (yellow); and meshless KNN (light blue).

The proposed meshless blending of KNN-PTV with c-RBFs demonstrates greater robustness at high frequencies, thanks to the regularization introduced through constrained regression and avoiding modulation effects due to moving averaging. This implies an increase in the cut-off frequency and more accurate reconstruction of small scales. Additionally, the regression via RBF improves the robustness against high-frequency noise contamination compared to other methodologies.

### 4.3 Modal analysis

The last part of the assessment involves a modal analysis conducted using POD via the method of snapshots (Sirovich, 1987). The reference data, along with those reconstructed through the different methodologies, have been decomposed to extract the POD modes.

Figure 7 displays the streamwise component of the first four dominant spatial modes  $\phi_i$ , depicted in the plane  $z/D = 0$  and normalized by their standard deviation ( $\sqrt{3N_p}$ ). The first two modes are associated with the convective motion of the vortex rings forming in the free shear layer (Violato and Scarano, 2013). These vortex rings are a characteristic feature of jet flows, particularly in transitional regimes, sustained by the Kelvin-Helmholtz mechanism of shear layer instability. As these structures travel downstream, they tend to interact and enter a precessing motion in pairs, often referred to as “leapfrogging” (Schram, 2003). This leapfrogging mechanism is represented in

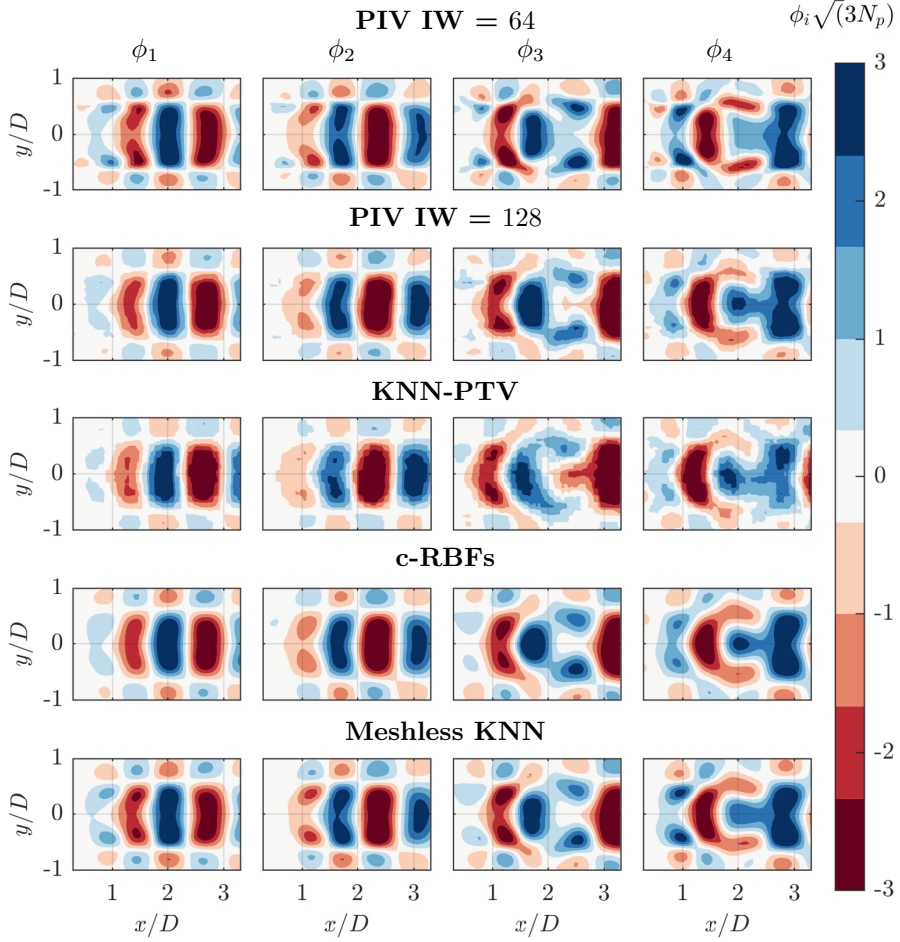


**Fig. 7** First 4 spatial modes  $\phi$  normalized with their standard deviation. First row: reference PIV with  $IW = 64$ ; second row: PIV with  $IW = 128$ ; third row: KNN-PTV; fourth row: c-RBFs; fifth row: Meshless KNN.

the third and fourth modes,  $\phi_3$  and  $\phi_4$ . During this process, the azimuthal modes grow rapidly, leading to the distortion of vortex filaments and their eventual breakup into smaller, three-dimensional fluctuations.

From a qualitative perspective, all the benchmark methods exhibit good agreement with the reference modes, accurately capturing the aforementioned mechanisms. As a general trend, the RBF-based approaches stand out as the methods that replicate these patterns with the highest accuracy, particularly in capturing the smallest scales, while the KNN-PTV appears to be the most affected by noise contamination. In modes 1 and 2, PIV with  $IW = 128$  and KNN-PTV fail to accurately model the first vortex pairs at  $x/D = 1$ : in these cases, the two methodologies completely miss the

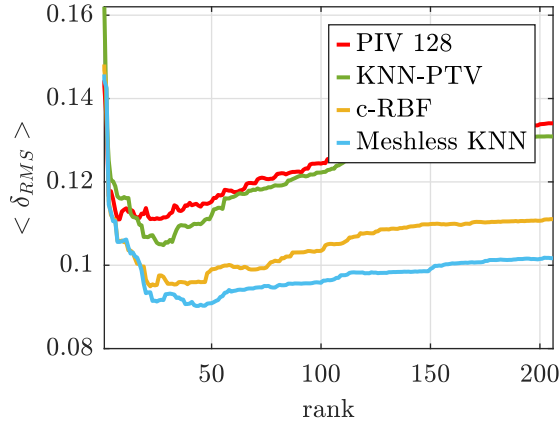


**Fig. 8** Root mean square error  $\langle \delta_{RMS} \rangle$  for varying rank  $r$ . The methodologies compared include: PIV with IW = 128 (red), KNN-PTV (green), c-RBFs (yellow) and meshless KNN (light blue).

external vortices and poorly model the internal ones. On the other hand, the RBF-based methods achieve the closest reconstruction, with the meshless KNN being also able to accurately reconstruct the shape of the modes and their velocity peaks. All of them completely miss the small vortices at the beginning of the region of interest. This is primarily due to the lack of particles and the dimensions of such structures, which make their recovery very challenging with traditional POD. The modulation effect on the data, once stored on an Eulerian grid, further hinders this process. A potential improvement in this regard could be achieved using meshless POD (Tirelli et al., 2025), but this lies beyond the scope of the present work. Modes 3 and 4 confirm the findings of the previous ones: once again, the meshless KNN exhibits the closest modes to the reference ones, successfully recovering the smallest scales and velocity peaks while maintaining the same shape as the reference modes.

The qualitative findings are confirmed by the reconstructed flow fields for varying rank  $r$ , reported in Fig. 5. The reconstructions are compared in terms of RMS error (computed as in Eq. (12)) at different ranks, where the meshless KNN once again achieves the highest accuracy across all ranks.

## 5 Conclusions

A novel meshless super-resolution technique has been introduced for image velocimetry, combining the strengths of KNN-PTV and constrained RBFs. Although presented in the context of particle image velocimetry, the technique is of general application to all cases in which data are sampled at scattered locations at different time instants (e.g. with random moving or on/off sensors). This method increases the density of scattered data by "borrowing" particles (or more generally, samples) from similar snapshots, even without time resolution, while strengthening regression robustness by enforcing physical constraints—all within a fully meshless framework. The results show promising improvements in both reconstruction accuracy and spatial resolution, validated through benchmark tests on experimental 3D measurements of a jet flow in air.

The main novelty of this approach is mesh independence, offering analytical representations of flow fields that can be easily interpolated and differentiated on any grid, enabling the extraction of high-resolution instantaneous fields and turbulence statistics. The technique is particularly advantageous for 3D flow analysis, where the demand for spatial resolution at reasonable computational costs is more critical compared to planar applications. Moreover, the use of constrained regression allows for handling larger interparticle spacing by enforcing flow-physics-based constraints.

The different analyses carried out in the paper demonstrate the following: first, the crucial role of physical constraints in regularising the reconstructed flow field to address the larger interparticle spacing typical of 3D scenarios; second, the artificial increase of particle density by borrowing particles from similar snapshots helps in the reconstruction of the smallest scales, especially in sparse cases (although its performance is depending on the regularisation in post-processing); last, the superiority of regression-based techniques (whether weighted or not) over simple moving averages (weighted or not).

It should also be noted that, while the methodologies examined may have reached their peak performance, the results of the fully meshless algorithm hold potential for further enhancement. Future studies will likely focus on identifying the optimal basis for flow field approximation, opening new avenues for improvement. Pressure estimation and the recovery of time resolution from data scattered in space and time are among the most straightforward applications of the method outside the primary scope of achieving high-resolution flow fields.

## Acknowledgment

This project has received funding from the European Research Council (ERC) under the European Union’s Horizon 2020 research and innovation programme (grant agreement No 949085, NEXTFLOW ERC StG). Views and opinions expressed are however those of the authors only and do not necessarily reflect those of the European Union or the European Research Council. Neither the European Union nor the granting authority can be held responsible for them.

L. Franceschelli is kindly acknowledged for providing the experimental dataset of the jet flow.

## References

- Tirelli, I., Ianiro, A., Discetti, S.: An end-to-end KNN-based PTV approach for high-resolution measurements and uncertainty quantification. *Experimental Thermal and Fluid Science* **140**, 110756 (2023)
- Tirelli, I., Mendez, M.A., Ianiro, A., Discetti, S.: A meshless method to compute the proper orthogonal decomposition and its variants from scattered data. *Proceedings of the Royal Society A* (2025) <https://doi.org/10.1098/rspa.2024.0526>
- Sperotto, P., Pieraccini, S., Mendez, M.A.: A meshless method to compute pressure fields from image velocimetry. *Measurement Science and Technology* **33**(9), 094005

(2022)

- Raffel, M., Willert, C.E., Scarano, F., Kähler, C.J., Wereley, S.T., Kompenhans, J.: Particle Image Velocimetry: a Practical Guide. Springer, ??? (2018)
- Westerweel, J., Elsinga, G.E., Adrian, R.J.: Particle image velocimetry for complex and turbulent flows. *Annual Review of Fluid Mechanics* **45**, 409–436 (2013)
- Sciacchitano, A., Scarano, F., Wieneke, B.: Multi-frame pyramid correlation for time-resolved PIV. *Experiments in Fluids* **53**, 1087–1105 (2012)
- Schneiders, J.F., Dwight, R.P., Scarano, F.: Time-supersampling of 3D-PIV measurements with vortex-in-cell simulation. *Experiments in Fluids* **55**, 1–15 (2014)
- Kähler, C.J., Scharnowski, S., Cierpka, C.: On the resolution limit of digital particle image velocimetry. *Experiments in Fluids* **52**, 1629–1639 (2012)
- Keane, R., Adrian, R., Zhang, Y.: Super-resolution particle imaging velocimetry. *Measurement Science and Technology* **6**(6), 754 (1995)
- Scarano, F.: Theory of non-isotropic spatial resolution in PIV. *Experiments in Fluids* **35**, 268–277 (2003)
- Ratz, M., Mendez, M.A.: A meshless and binless approach to compute statistics in 3D Ensemble PTV. *Experiments in Fluids* **65**, 142 (2024)
- Mendez, M.A., Den Berghe, J., Ratz, M., Fiore, M., Schena, L.: Tutorials on physics-constrained regression. In: Mendez, M.A., Parente, A. (eds.) *Machine Learning for Fluid Dynamics*. VKI Lecture Series, ??? (2025). Chap. 3. Lecture notes from the VKI LS
- Meinhart, C.D., Wereley, S.T., Santiago, J.G.: A PIV algorithm for estimating time-averaged velocity fields. *J. Fluids Eng.* **122**(2), 285–289 (2000)
- Westerweel, J., Geelhoed, P., Lindken, R.: Single-pixel resolution ensemble correlation for micro-PIV applications. *Experiments in Fluids* **37**(3), 375–384 (2004)
- Scharnowski, S., Hain, R., Kähler, C.J.: Reynolds stress estimation up to single-pixel resolution using PIV-measurements. *Experiments in Fluids* **52**, 985–1002 (2012)
- Cowen, E., Monismith, S., Cowen, E., Monismith, S.: A hybrid digital particle tracking velocimetry technique. *Experiments in Fluids* **22**(3), 199–211 (1997)
- Agüera, N., Cafiero, G., Astarita, T., Discetti, S.: Ensemble 3D PTV for high resolution turbulent statistics. *Measurement Science and Technology* **27**(12), 124011 (2016)
- Discetti, S., Liu, Y.: Machine learning for flow field measurements: a perspective.

- Measurement Science and Technology **34**(2), 021001 (2022)
- Cortina-Fernández, J., Sanmiguel Vila, C., Ianiro, A., Discetti, S.: From sparse data to high-resolution fields: ensemble particle modes as a basis for high-resolution flow characterization. *Experimental Thermal and Fluid Science* **120**, 110178 (2021)
- Deng, Z., He, C., Liu, Y., Kim, K.C.: Super-resolution reconstruction of turbulent velocity fields using a generative adversarial network-based artificial intelligence framework. *Physics of Fluids* **31**(12) (2019)
- Güemes, A., Sanmiguel Vila, C., Discetti, S.: Super-resolution generative adversarial networks of randomly-seeded fields. *Nature Machine Intelligence* **4**(12), 1165–1173 (2022)
- Cai, S., Zhou, S., Xu, C., Gao, Q.: Dense motion estimation of particle images via a convolutional neural network. *Experiments in Fluids* **60**, 1–16 (2019)
- Lagemann, C., Lagemann, K., Mukherjee, S., Schröder, W.: Deep recurrent optical flow learning for particle image velocimetry data. *Nature Machine Intelligence* **3**(7), 641–651 (2021)
- Yu, C., Bi, X., Fan, Y., Han, Y., Kuai, Y.: LightPIVNet: An effective convolutional neural network for particle image velocimetry. *IEEE Transactions on Instrumentation and Measurement* **70**, 1–15 (2021)
- Schröder, A., Schanz, D.: 3D Lagrangian Particle Tracking in Fluid Mechanics. *Annual Review of Fluid Mechanics* **55** (2023)
- Schneiders, J.F., Scarano, F.: Dense velocity reconstruction from tomographic PTV with material derivatives. *Experiments in Fluids* **57**, 1–22 (2016)
- Buhmann, M.D.: Radial basis functions. *Acta numerica* **9**, 1–38 (2000)
- Lumley, J.L.: The structure of inhomogeneous turbulent flows. *Atmospheric turbulence and radio wave propagation*, 166–178 (1967)
- Sperotto, P., Ratz, M., Mendez, M.A.: SPICY: a Python toolbox for meshless assimilation from image velocimetry using radial basis functions. *Journal of Open Source Software* **9**(93), 5749 (2024)
- Tirelli, I., Solera-Rico, A., Guemes, A., Vila, C.S., Ianiro, A., Discetti, S.: Assessment of data-driven 3D PTV techniques. In: *Proceedings of the 15th International Symposium on Particle Image Velocimetry* (2023)
- Mendez, M.A., Raiola, M., Masullo, A., Discetti, S., Ianiro, A., Theunissen, R., Buchlin, J.-M.: POD-based background removal for particle image velocimetry. *Experimental Thermal and Fluid Science* **80**, 181–192 (2017)

- Wieneke, B.: Volume self-calibration for 3D particle image velocimetry. *Experiments in Fluids* **45**(4), 549–556 (2008)
- Elsinga, G.E., Scarano, F., Wieneke, B., Oudheusden, B.W.: Tomographic particle image velocimetry. *Experiments in Fluids* **41**(6), 933–947 (2006)
- Discetti, S., Astarita, T.: A fast multi-resolution approach to tomographic PIV. *Experiments in Fluids* **52**, 765–777 (2012)
- Atkinson, C., Soria, J.: An efficient simultaneous reconstruction technique for tomographic particle image velocimetry. *Experiments in Fluids* **47**(4), 553–568 (2009)
- Novara, M., Scarano, F.: A particle-tracking approach for accurate material derivative measurements with tomographic piv. *Experiments in Fluids* **54**, 1–12 (2013)
- Raiola, M., Discetti, S., Ianiro, A.: On PIV random error minimization with optimal POD-based low-order reconstruction. *Experiments in Fluids* **56**, 1–15 (2015)
- Hunt, J.C., Wray, A.A., Moin, P.: Eddies, streams, and convergence zones in turbulent flows. *Studying turbulence using numerical simulation databases, 2. Proceedings of the 1988 summer program* (1988)
- Savitzky, A., Golay, M.J.: Smoothing and differentiation of data by simplified least squares procedures. *Analytical chemistry* **36**(8), 1627–1639 (1964)
- Sirovich, L.: Turbulence and the dynamics of coherent structures. i. coherent structures. *Quarterly of Applied Mathematics* **45**(3), 561–571 (1987)
- Violato, D., Scarano, F.: Three-dimensional vortex analysis and aeroacoustic source characterization of jet core breakdown. *Physics of Fluids* **25**(1) (2013)
- Schram, C.F.: Aeroacoustics of subsonic jets: prediction of the sound produced by vortex pairing based on particle image velocimetry (2003)